NJC

PAPER

View Article Online
View Journal | View Issue

Cite this: *New J. Chem.*, 2019, 43, 12923

Direct growth of oriented nanocrystals of gamma-iron on graphene oxide substrates. Detailed analysis of the factors affecting unexpected formation of the gamma-iron phase†

Artur Khannanov, [a] Airat Kiiamov, [ab] Alina Valimukhametova,[a] Farit G. Vagizov*[b] and Ayrat M. Dimiev *[a]

Received 4th June 2019,
Accepted 16th July 2019

DOI: 10.1039/c9nj02903f

rsc.li/njc

In bulk, face-centered gamma-iron exists only at temperatures above 917 °C, returning back to body-centered alpha-iron upon cooling below this temperature. In this work, we report formation of the gamma-iron phase at temperatures significantly lower than the 917 °C threshold in the form of nanoparticles. Moreover, the as-grown nanoparticles have specific orientation along the (002) plane as the result of the templating effect of the graphene oxide substrate. Also, we provide a complete account of the factors responsible for the formation of the gamma-phase. Namely, we demonstrate the role of the type of carbon substrate, and the effect of the temperature and time of annealing and the graphene oxide/iron ion ratio. We demonstrate that the gamma-phase is not formed when using three-dimensional forms of carbon, elucidating the "magic" role of graphene oxide in this process.

Introduction

Composite materials comprising metal nanoparticles (NPs) on a structural support have gained significant attention in recent years as novel systems for new generations of catalysts, electrode materials in energy conversion/storage devices, and similar applications. Due to their high surface area, these nanostructured systems possess apparent advantages over traditional forms of materials due to the lower cost–performance ratio. Such composite materials are normally grown *in situ* from solutions of soluble salts of target metals in the presence of structural supports. Chemical reducing agents are needed to convert the metals to the zero-valent states. Another less frequently used strategy is the thermal decomposition of metal-containing compounds. A combination of different approaches is also frequently used. The exact strategy is often chosen based on the standard reduction potential of a particular metal, *i.e.* on its ability to be reduced.

The use of carbon materials as a structural support for nanoparticles has a number of key advantages, namely, a large specific surface area, low cost and ease of use. All carbon nanomaterials are capable of holding nanoparticles on themselves; there are reports of nanoparticle fixation on the surface of fullerenes,[1,2] single-walled,[3,4] and multi-walled carbon nanotubes,[5–7] graphene nanoribbons,[8] graphene,[9,10] and graphene oxide (GO).[11–13]

Of all carbon nanomaterials, graphene oxide is the most interesting platform for the growth of nanoparticles. Unlike other forms of carbon, GO contains oxygen functional groups that facilitate uniform deposition of metals on its surface and formation and stabilization of metal clusters.[14] Another advantage of GO over its non-oxidized analogue is its ability to form stable solutions in several solvents, by exfoliating to single-atomic-layer sheets.[15] The solution phase provides easy and unimpeded access of reactants to the GO surface, opening unlimited avenues for liquid phase processing. This property of GO makes it possible to form germs of metal nanoclusters on the GO surface from ions present in bulk salt solution. Since in solution the GO sheets are surrounded by an excess of metal ions, nanoparticles easily assemble themselves over the entire surface area.

Among other metals, iron nanoparticles are of the greatest interest of researchers. This is primarily due to the wealth of properties and practical applications of nanoparticles of zero-valent iron (ZVI),[16] iron alloys[17] and iron oxides.[18] The magnetic properties of iron nanoparticles have been studied most thoroughly and completely.[19] Of undoubted interest are the catalytic properties of iron nanoparticles, since they can replace platinum or palladium in several reactions.[20,21] Since iron nanoparticles are not toxic, they are widely used in the biomedical field. However, the formation of iron nanoparticles and their transitions from one form to another have not been yet fully studied.

[a] *Laboratory for Advanced Carbon Nanomaterials, Kazan Federal University, Russian Federation. E-mail: AMDimiev@kpfu.ru*
[b] *Institute of Physics, Kazan Federal University, Kremlyovskaya str. 18, Kazan 420008, Russian Federation. E-mail: vagizovf@gmail.com*

† Electronic supplementary information (ESI) available. See DOI: 10.1039/c9nj02903f

In the bulk macroscopic form, iron exhibits polymorphism and has four types of crystal lattices. Up to 769 °C iron exists in its alpha-form (α-Fe), also called ''ferrite'', with a body-centered cubic lattice and the properties of a ferromagnet (the Curie point is 769 °C ≈ 1043 K). In the temperature range 769–917 °C, beta-iron (β-Fe) exists, which differs from α-Fe only in its paramagnetic properties. Currently, the alpha and beta forms are often considered as one type of iron, *i.e.* as α-Fe, due to the same body-centered crystalline structure. At 917 °C, α-Fe transforms into a face-centered cubic lattice called γ-Fe (or austenite) with diamagnetic properties. Austenite, due to its more open structure, can incorporate up to 2.03% carbon. When the temperature is lowered below 917 °C, carbon atoms diffuse out of the structure, and γ-Fe turns back into α-Fe. The origin of the α-to-γ or γ-to-α transitions is largely unknown even for the bulk forms of iron. However, at room temperature, bulk iron exists only in its alpha-form. The same is generally true for nanoforms of iron. In most of the literature studies, formation of iron oxides and carbides but not ZVI was reported.

Thus, impregnation of activated carbon and carbon black with iron pentacarbonyl and subsequent annealing yields a mixture of iron oxides and α-Fe.[22] Wang *et al.* annealed a GO–$Fe(NO_3)_3$ composite and reported formation of iron oxides and metallic Fe, but did not specify the type of the formed iron.[23] Formation of Fe_3C was reported in two independent studies upon thermal annealing of GO impregnated with $FeCl_3$ in the presence of dopamine.[24,25] Formation of iron oxides Fe_2O_3 and Fe_3O_4 was reported upon thermal annealing of GO impregnated with iron(II) sulfate $FeSO_4{\cdot}7H_2O$.[26] Lv *et al.* obtained hybrid iron nanoparticles (nanosacks) from FeOOH nanorods by spraying a microemulsion with GO solution through a furnace.[27] Thus, to the best of our knowledge, formation of γ-Fe on a GO support has not been reported before. We can only mention the very recent study by Zhang *et al.*, reporting formation of γ-Fe in a non-specified quantity by annealing a $Fe(NO_3)_3$/lignin mixture.[28] From these perspectives, our most recent result reporting formation of room-temperature stable γ-Fe by annealing GO–$Fe(NO_3)_3$ composites was very surprising.[12] The γ-Fe phase was stabilized in the form of nanoparticles (NPs) with a complex core–shell structure. The γ-Fe core contained up to 1.5% carbon, and a thin layer of Fe/C solid solution on the surface served as the buffer, controlling the carbon content in the core. γ-Fe might be very interesting as a new catalytic system. For example, Khasanov *et al.* demonstrated that the γ-Fe phase plays a crucial role in the catalytic growth of carbon nanotubes.[29]

However, the key factors responsible for the formation of this phase still remain unknown. The aim of this work was to investigate the role of four factors: the type of carbon substrate, the reaction temperature and time, and the GO/Fe ratio.

Experimental

The experimental design and tested factors (Fig. 1)

Experiments with alternative carbon sources

Preparation of OMC. To prepare the oxidized forms of the three carbon sources (OMC), we used the same methods as in ref. 30. First, we prepared 88.6% sulfuric acid by diluting 150 g of 96% commercial sulfuric acid with 12.5 g of DI water. The diluted acid was cooled to room temperature. 10.0 g of the carbon source was poured into the 88.6% sulfuric acid with stirring. Potassium permanganate ($KMnO_4$) was poured in two portions of 6.0 g each with a 1 h interval. The reaction mixture was continuously stirred for 12 h after pouring the last $KMnO_4$ portion. Next, the reaction was quenched with 500 mL of DI water, and the diluted reaction mixture was filtered to separate the as-formed OMC product from the acidic waste. The OMC collected from the filter was redispersed in 500 mL of DI water and stirred for 30 min with a magnetic stirrer, and the dispersion was filtered to separate the purified OMC. The above mentioned purification procedure was repeated 4 times. The filtrate was always transparent and colorless, which indicates that very little submicron-scale particles were dispersed in the water, and that the carbon did not crush to smaller fragments even during magnetic stirring. After the 5th washing, the pH of the filtrate was ∼5, indicating removal of practically all sulfuric acid.

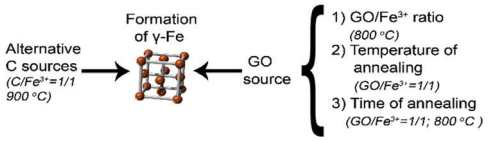

Fig. 1 The schematic of the experimental design.

Preparation of C/Fe^{3+} and OMC/Fe^{3+} composites (impregnation step). For the synthesis of the C/Fe^{3+} and OMC/Fe^{3+} composites, $Fe(NO_3)_3$ solution (20 mL, 2%) was added to a C or OMC dispersion in water (20.0 mL, 2.0%) with stirring. The dispersion was further stirred using a magnetic stirrer for 24 h. After impregnation, the solution was filtered through a membrane filter with a pore diameter of 1 μm using a vacuum. The filter cake was re-dispersed in 1000 mL of water, and was re-filtered after 2 h of mixing. This procedure was performed twice. After that, the samples were dried under ambient conditions and used as air-dried solid samples.

Annealing of C/Fe^{3+} and OMC/Fe^{3+} composites. The air-dried C/Fe^{3+} and OMC/Fe^{3+} were introduced into a tube furnace purged with nitrogen to remove all oxygen and were heated to the selected temperature. The heating rate was 10 °C min^{-1}. The sample was kept at the selected temperature for 120 min. Then, the oven was turned off and cooled down naturally to ∼100 °C in the flow of nitrogen. After cooling, the sample was removed from the oven and used for characterization.

Experiments with graphene oxide

Synthesis of graphene oxide. Graphite flakes (10 g, 832 mmol) were dispersed in 96% sulfuric acid (680 mL) at room temperature using a mechanical stirrer. After 10 min of stirring, 1 wt equiv. of $KMnO_4$ (10 g, 63.2 mmol) was added. The mixture became green due to the formation of the MnO_3^+ oxidizing agent. Additional portions of $KMnO_4$ (10 g, 63.2 mmol of each) were added when the green color of MnO_3^+ was diminished indicating that the oxidizing agent was consumed. In total, 4 wt equiv. of $KMnO_4$

was sequentially added. The end of the reaction was determined by the disappearance of the green color after adding each $KMnO_4$ portion. After full consumption of $KMnO_4$, the reaction was diluted with 1400 mL of an ice–water mixture, and then H_2O_2 solution (16 mL, 30%) was added to convert the manganese by-products to soluble colorless Mn(II) ions. The reaction mixture was centrifuged for 15 min at 8900 rpm to separate GO from the acid. For purification, the GO precipitate was redispersed in distilled water, stirred for 30 min, and centrifuged for 20 min at 8900 rpm to separate purified GO from the washing water. This procedure constitutes one purification cycle. Next four purification cycles were performed consecutively: the first time with distilled water and three times with HCl (4%). The GO precipitate after the last washing was dried in the air. 18.2 g of air-dried GO was obtained.

The growth of the iron nanoparticles (Fe-NP) on the GO substrate. The growth of Fe-NP was conducted in two steps: (1) liquid phase impregnation of GO with Fe^{3+} ions to form GO/Fe^{3+} composites, and (2) thermal annealing of the as-formed GO/Fe^{3+} composites to yield iron nanoparticles on the thermally-processed GO substrate (tpGO–Fe-NP).

Preparation of GO/Fe^{3+} composites (impregnation step)

Excess iron content. For the synthesis of GO/Fe^{3+} composites with a ratio of 1/0.75, $Fe(NO_3)_3$ solution (20 mL, 2%) was added to GO solution (20.0 mL, 2.7%) with stirring. The dispersion was further stirred using a magnetic stirrer for 24 h. For the synthesis of GO/Fe^{3+} composites with a ratio of 1/0.5, 20 mL of 1% $Fe(NO_3)_3$ solution was added to GO solution (20.0 mL, 2%) with stirring. The dispersion was further stirred using a magnetic stirrer for 24 h. In this experiment, the separation of overage Fe^{3+} ions by centrifugation was not carried out. After that, the jelly samples were dried under ambient conditions and used as air-dried solid samples.

Low iron content. For the synthesis of GO/Fe^{3+} composites with ratios of 2.5/1, 5/1, 10/1, 20/1, 40/1 and 80/1, $Fe(NO_3)_3$ solutions (20 mL) with concentrations of 0.4%, 0.2%, 0.1%, 0.05%, 0.025% and 0.0125%, respectively, were added to GO solution (20.0 mL, 2%) with stirring. The dispersion was further stirred using a magnetic stirrer for 24 h. After that, the jelly samples were dried under ambient conditions and used as air-dried solid samples.

Typical iron content. For the synthesis of GO/Fe^{3+} composites, $Fe(NO_3)_3$ solution (20 mL, 2%) was added to GO solution (20.0 mL, 2.0%) with stirring. The dispersion was further stirred with a magnetic stirrer for 24 h. The resulting dispersion was centrifuged for ~40 min at 5000 rpm until complete separation of the composite product, and the supernatant was decanted. For purification, the jelly Fe/GO precipitate was redispersed in 400 mL of DI water, stirred for 30 min and centrifuged as above. This constitutes one purification cycle. Six purification cycles were performed. The purified jelly samples were dried under ambient conditions and used as air-dried solid samples.

The growth of Fe-NPs (annealing). The air-dried GO/Fe^{3+} samples were introduced into a tube furnace purged with nitrogen to remove all the oxygen, and heated to a selected temperature. The heating rate was 5 °C min^{-1}. All samples, except for the samples used to study the effect of time, were annealed at the selected temperature for 120 min. Then, the oven was turned off and cooled down naturally to ~100 °C in the flow of nitrogen. After cooling, the sample was removed from the oven and used for characterization.

Characterization of the obtained samples

Scanning electron microscopy (SEM) images were acquired with a field-emission high resolution scanning electron microscope Merlin from Carl Zeiss at an acceleration voltage of incident electrons of 5 kV and a probe current of 300 pA.

Transmission electron microscopy (TEM) imaging and electron diffraction were performed with a Hitachi HT7700 electron microscope at an electron acceleration voltage of 100 kV.

Powder X-ray diffraction (XRD) was performed with a Bruker D8 Advance with Cu Kα radiation (λ = 1.5418 Å) in the Bragg–Brentano geometry; the rate was 0.18° min^{-1}; the range of 2Θ angles was from 7° to 100°; and the step was 0.015°.

Thermogravimetric analysis (TGA) data were measured with an STA 449 F5 Jupiter analyzer from Netzsch in both Ar and synthetic air atmospheres.

FTIR spectra were measured with a Spectrum 400 FT-IR spectrometer (PerkinElmer Inc.) with a Diamond KRS-5 attachment with attenuated total internal reflectance (resolution 0.5 cm^{-1}, 32 scans, wavelength range 4000–400 cm^{-1}).

Mössbauer effect measurements were carried out mainly at room temperature using a conventional constant-acceleration spectrometer made by WissEl (Germany). A commercial Mössbauer source of ^{57}Co in a rhodium matrix (Ritverc Isotope Products, Saint Petersburg, Russia) with an activity of about 40 mCi was used as a γ-radiation source. The experimental spectra were least-squares fitted with the assumption that the line shapes are Lorentzian to yield hyperfine parameters, namely the isomer shift (IS), quadrupole splitting (QS), and hyperfine field (HHF). Metallic-iron foil at RT was used for velocity calibration of the Mössbauer spectrometer. Isomer shifts were referenced to α-Fe at RT.

Materials

Sulfuric acid was from Shchekinoazot LLC, Russia; hydrochloric acid and nitric acid were from CJSC TatKhimProduct, Russia; potassium permanganate was from MCD Company, Russia; and iron(III)nitrate nonahydrate was from Acros Organics, Spain. The graphite was natural flaky graphite, GL-1 grade. The carbon source C1 was the commercially available C-seal-F from MiS-WACO company, USA; the carbon source C2 was a sample of a carbon-based mineral, mined in the Karelia Republic region, Russian Federation; and the carbon source C3 was a bituminous coal sample mined in the Kuznetsk Basin, Russia.

Results and discussion

The role of the carbon support

To evaluate the role of graphene oxide, we carried out reactions with other forms of both oxidized and non-oxidized carbon.

As carbon materials, we used C-seal-F (C1) and Shungit (C2), two carbon sources previously tested as sorbents of metal cations,[30] and bituminous coal (C3). The oxidatively modified forms, denoted as OMC1–OMC3, respectively, were also prepared and tested. The temperature program of thermal reduction, used here and hereinafter, is presented in the ESI† section.

For non-oxidized carbon (Fig. S1, ESI†), none of the as-obtained products show the formation of face-centered iron. The XRD diffraction pattern of the C1-based sample contains only carbon reflections (Fig. S1a, ESI†). The diffraction patterns of the C2 and C3-based samples contain weak signals of α-Fe (Fig. S1b and c, ESI†). The Mössbauer spectrum of C1–Fe-NP shows an extremely weak signal (Fig. S1d, ESI†) due to the very low sorption of iron by non-oxidized carbon. In the samples C2–Fe-NP and C3–Fe-NP, Mössbauer spectroscopy confirms the presence of alpha iron in very low quantities (Fig. S1e–f, ESI†). In addition, an oxide phase is present in them, which corresponds to Fe_2O_3. The thermogravimetric data (Fig. S1g–i, ESI†) confirm an extremely low amount of iron (1.5–3.5%) in all the three samples. Thus, the non-oxidized carbon materials absorb very little iron, and do not afford formation of γ-Fe.

In the next step, we studied the oxidized forms (OMC) of the same carbon materials. The quantity of the absorbed iron was slightly increased, compared to the non-oxidized forms, however, no significant changes in the composition of the formed iron phases were observed (Fig. S2, ESI†). In the OMC2 and OMC3 samples, some form of iron was formed that, based on the Mössbauer data, can be attributed to γ-Fe, but its content did not exceed 10% of all the iron present in the sample (Fig. S2e and f, ESI†). Thus, the three tested carbon materials and their oxidized forms do not lead to formation of the face-centered form of iron. Thus, GO is a unique material affording formation of γ-Fe. Most likely the uniqueness of GO is related to two main factors. The first factor is the large and uniformly oxidized surface of GO, on which iron ions can be properly organized during the impregnation step. The second factor is the single-layer structure of GO. In the process of thermal reduction, the growth of nanocrystals occurs by the directional migration of nanoparticles along the surface and between the layers of graphene.[11]

The role of the GO/Fe ratio

The next factor we investigate is the role of the initial GO/Fe^{3+} ratio during the impregnation step. In previous work,[12] we removed the excess Fe^{3+} ions from the solution by cyclic dissolution and precipitation of GO/Fe^{3+}, until there were no Fe^{3+} ions in the supernatant, which was tested with $K_4[Fe(CN)_6]$. Thus, the quantity of the Fe^{3+} ions was limited by the sorption capacity of GO. Therefore, in this work, it was important to study the reaction at different GO/Fe^{3+} ratios both with an excess of and limited Fe^{3+} ions. For the excess conditions, GO/Fe^{3+} ratios 1.33/1 (R1) and 2/1 (R2) were selected, which correspond to the ratio obtained after the second and third rinsing of the composite in ref. 12. The annealing temperature was 800 °C and the annealing time was 2 hours. Fig. 2 shows the XRD and Mössbauer spectra of the as-obtained products at the R1 ratio (tpGO–Fe-R1) and R2 ratio (tpGO–Fe-R2). According to the XRD patterns (Fig. 2a), two main

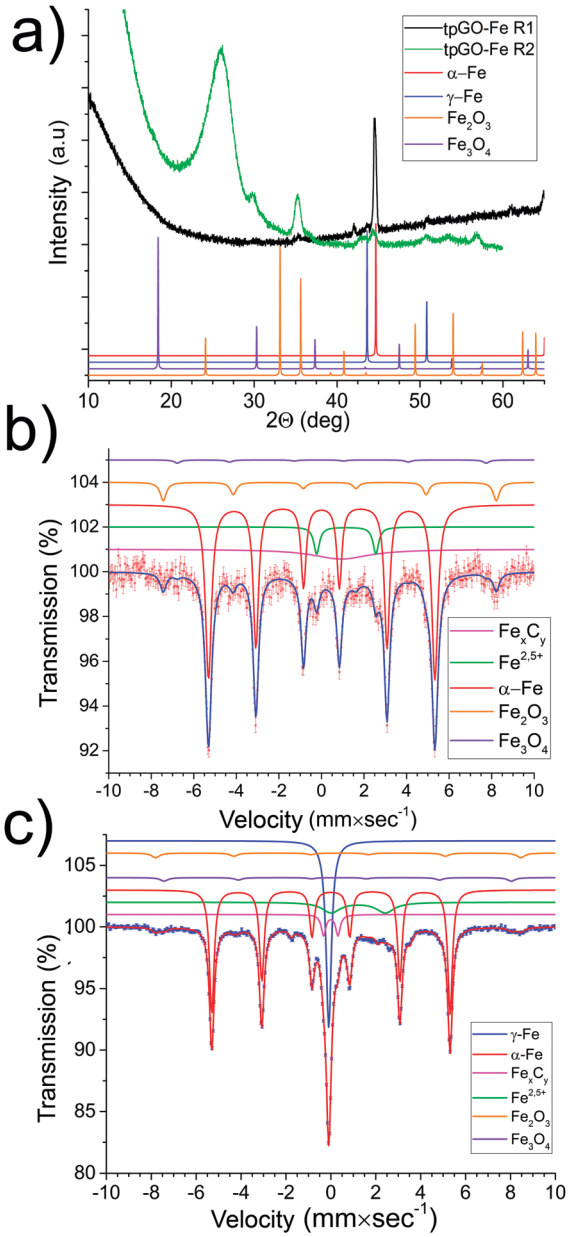

Fig. 2 Characteristics of the tpGO–Fe composites obtained at low GO/Fe ratios. (a) XRD patterns of tpGO–Fe-R1 and tpGO–Fe-R2, (b) Mössbauer spectra of tpGO–Fe-R1 and (c) Mössbauer spectra of tpGO–Fe-R2.

conclusions can be drawn. First, the formation of α-Fe with traces of γ-Fe and iron oxides is observed. Secondly, there is no graphitic signal in the range 23–25° of 2Θ, suggesting destruction of the carbon substrate. A decrease in the concentration of Fe^{3+} ions significantly reduces the destruction of the substrate, and leads to the formation of γ-Fe. This trend is also confirmed by the Mössbauer spectroscopy data (Fig. 2b). The spectrum of tpGO–Fe-R1, besides other components, has a strongly broadened line with a center at a velocity of 0.92 mm × s^{-1}, which can be attributed to iron atoms in the fine particles of the solid iron/carbon solutions, or metastable carbide phases. The content of this component is about 9%. The spectrum of tpGO–Fe-R1 contains also a doublet and three sextets. The doublet with IS = 1.16 and

QS = 2.78 mm × s^{-1} most likely corresponds to Fe^{2+} (5%). The first sextet (76%) corresponds to α-Fe and the remaining two sextets correspond to Fe_2O_3 (8%) and Fe_3O_4 (~1%). In the spectra of tpGO–Fe-R2 (Fig. 2c), a significant increase in the γ-Fe and a decrease in the α-Fe amount are observed. Thus, the "excess" of iron ions in the initial composite leads to the formation of the α-Fe phase. The low carbon content in the system does not allow stabilization of the nanoparticles, and destroys the tpGO substrate.

Since the increase of the iron content does not lead to the formation of the target product (γ-Fe), it is logical to shift the ratio toward lower metal content. Six different GO/Fe^{3+} ratios were used: 2.5/1 (R3), 5/1 (R4), 10/1 (R5), 20/1 (R6), 40/1 (R7) and 80/1 (R8). Note that for the last three ratios the GO solution did not coagulate after the addition of the iron salt. All the six GO/Fe^{3+} composites were thermally reduced synchronously. Fig. 3 presents the XRD patterns (Fig. 3a and c) and the Mössbauer spectra (Fig. 3b and d) of the obtained samples. A decrease in the initial GO/Fe^{3+} ratio facilitates the formation of the γ-Fe phase. In all the six samples, the singlet with IS = −0.06 mm × s^{-1} associated with γ-Fe is present (Fig. 3b).

The content of this form increases from 22% for tpGO–Fe-R3 to 42.5% for tpGO–Fe-R8 (Table 1). In addition to the growth of γ-Fe, there is an increase in the iron phase, which we attribute to the fine particles of the Fe_xC_y solid solution.

It is quite interesting that in tpGO–Fe-R3 there are two different iron oxides: Fe_2O_3 (12%) and Fe_3O_4 (18%), while in tpGO–Fe-R4 and tpGO–Fe-R5 there is only Fe_2O_3 with a content of 26% and 35%, respectively. At the same time, a gradual decrease in the α-Fe content is observed in the three samples (Table 1).

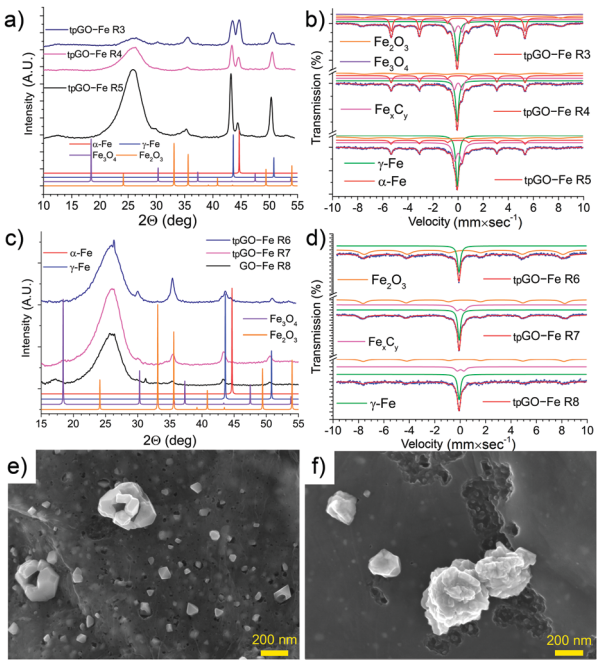

Fig. 3 Characteristics of the tpGO–Fe composites obtained at high GO/Fe ratios. (a) XRD spectra of tpGO–Fe-R3–R5; (b) Mössbauer spectra of tpGO–Fe-R3–R5; (c) XRD spectra of tpGO–Fe-R6-R8; (d) Mössbauer spectra of tpGO–Fe-R6-R8; (e) SEM image of tpGO–Fe-R5; and (f) SEM image of tpGO–Fe-R7. The annealing temperature is 800 °C.

Table 1 The content of different types of iron in tpGO–Fe samples obtained at different GO/Fe^{3+} ratios according to the Mössbauer spectroscopy data (%)

	γ-Fe	α-Fe	Fe_xC_y	Fe_3O_4	Fe_2O_3
tpGO–Fe-R3	22	32	16	12	18
tpGO–Fe-R4	28	23.5	19	3	26
tpGO–Fe-R5	30	10	26		34
tpGO–Fe-R6	28	Broad signals, low accuracy of determination			
tpGO–Fe-R7	32		21		47
tpGO–Fe-R8	43		19		38

Therefore, we suggest that several chemical reactions occur simultaneously during the thermal reduction (eqn (1) and (2)).

$$Fe_2O_3{\cdot}FeO + C \rightarrow Fe_2O_3 + \alpha Fe + CO \quad (1)$$

$$\alpha Fe + C_{tpGO} \rightarrow Fe_xC_y \rightarrow \gamma Fe + C_{graphene} \quad (2)$$

Eqn (1) shows the classical reduction of magnetite by carbon. It explains why the content of the Fe_2O_3 phase increases with the GO/Fe^{3+} ratio.

A decrease in the α-Fe content is associated with the second process (eqn (2)). In this step, carbonization of iron occurs with the formation of the Fe_xC_y phase. Accordingly, the higher the carbon content, the faster and more efficient the process of converting α-Fe to solid solution Fe_xC_y, from which γ-Fe is subsequently formed.

For the samples tpGO–Fe-R6 to tpGO–Fe-R8, the α-Fe phase is no longer observed, either in Mössbauer spectroscopy (Fig. 3d) or in the XRD data (Fig. 3c). For tpGO–Fe-R6 (Fig. 3c), the γ-Fe, Fe_2O_3 and Fe_3O_4 reflections are observed and the α-Fe signal is at the noise level. For R7, only γ-Fe, Fe_2O_3 and Fe_3O_4 reflexes (Fig. 3c) are observed. For tpGO–Fe-R8, only γ-Fe reflections and weak Fe_2O_3 signals are registered.

The percentage of the γ-Fe signal increases in the series tpGO–Fe-R6–R7–R8 (Table 1). Note that the content of the Fe_xC_y phase for R7 and R8 is about the same (~20%), but the amount of the oxide is reduced from 47% to 38%. At the same time, compared to tpGO–Fe-R7, in tpGO–Fe-R8 the γ-Fe content is increased by 11%, while α-Fe was not present in both samples. Thus, we are witnessing the transformation of oxides directly to face-centered iron. Thus, for the higher GO/Fe^{3+} ratios, the γ-Fe formation mechanism can be represented as eqn (3):

$$Fe_2O_3 + C_{tpGO} \rightarrow Fe_xC_y + CO_2 \rightarrow \gamma Fe + C_{graphene} \quad (3)$$

This conclusion is also confirmed by the SEM images of tpGO–Fe-R5 and tpGO–Fe R7 (Fig. 3e and f). For tpGO–Fe-R5, there are 2 types of particles (Fig. 3e). Large particles with a mixed crystal structure are most likely γ-Fe-NPs. Small particles, in their majority, have the form of a tetragonal bipyramid. This form of crystals is inherent to hematite. The content of these particles has been significantly decreased in tpGO–Fe-R7 (Fig. 3f), while the content of the large polycrystalline particles is increased compared to tpGO–Fe-R5. Thus the γ-Fe phase grows at the expense of the oxide phase. As the summative effect, in the series tpGO–Fe-R3 to tpGO–Fe-R8, the content of γ-Fe increases 2 times, and reaches the limit for the given annealing conditions.

To conclude this section, increasing the initial GO/Fe^{3+} ratio facilitates the formation of γ-Fe-NPs. However, even with an 80-fold excess of GO, the pure γ-phase has been not obtained. The process of the γ-Fe formation depends not only on the initial GO/Fe^{3+} ratio, but also on the temperature and time of thermal treatment, as we discussed above. Thus, the next step of the work was the study of the effect of the annealing time and temperature on the formation of γ-Fe.

The role of the annealing temperature

In this series of experiments, the original GO/Fe^{3+} ratio was 1/1 by weight. The excess of the unabsorbed Fe^{3+} ions was completely removed as in our previous work.[12] In that work,[12] we studied the same GO/Fe^{3+} sample, which had been repetitively subjected to several cycles of cooling and heating at progressively higher temperatures. Therefore, it was impossible to accurately assess the effect of the temperature and time of annealing on the formation of the γ-Fe phase. However, γ-Fe was observed for the first time in sufficient quantities after heating at 750 °C.[12] In this work, to investigate the role of the annealing temperature, three samples were prepared by annealing at 750, 800, and 900 °C. In all the three samples, after 2-hour annealing, the formation of γ-Fe, α-Fe, a set of iron oxides, and Fe_xC_y solid solution was observed both by Mössbauer spectra (Fig. 4a) and XRD (Fig. 4b). There is a steady increase in the content of the target phase with increasing temperature, which is consistent with the previous data. The γ-Fe content is 25%, 40%, and 48.5% for the isotherms at 750, 800, and 900 °C, respectively (Table 2). This observation is in line with our previous work[12] and with the study by Zhang *et al.*[28]

Table 2 The content of different types of iron in GO/Fe^{3+} samples annealed at different temperatures according to the Mössbauer spectroscopy data (%)

	γ-Fe	α-Fe	Fe_xC_y	Fe_3O_4	Fe_2O_3
tpGO–Fe/NP-750	25	51	16	4	4
tpGO–Fe/NP-800	40	16	15	6	23
tpGO–Fe/NP-900	48	12	12	10	18

An additional interesting observation have been made. In all the XRD spectra discussed above, as well as in those presented in our previous study,[12] the intensities of the γ-Fe reflexes were in accordance with the standard distribution for powder samples. The same distribution is observed in this experiment for the samples obtained by annealing at 750 and 900 °C. However, for the sample obtained at 800 °C, an unusually high intensity of the (200) signal is registered. This observation is related to the specific orientation of the as-grown nanocrystals on a flat tpGO substrate.

This conclusion is supported by the SEM images. Many particles obtained with the 800 °C isotherm have a cubic shape, lying flat on the tpGO substrate (Fig. 4c and d), which explains their orientation along the 200 plane. This is not the case for the sample obtained at 900 °C (Fig. 4e and f). Usually, the growth of oriented particles requires specific conditions and a directing substrate, such as a metal treated in a specific way.[31–33] In this study, we witness another advantage of graphene oxide. It not only affords formation of room-temperature stable γ-Fe, but also templates the growth of γ-Fe nanoparticles in a specific direction.

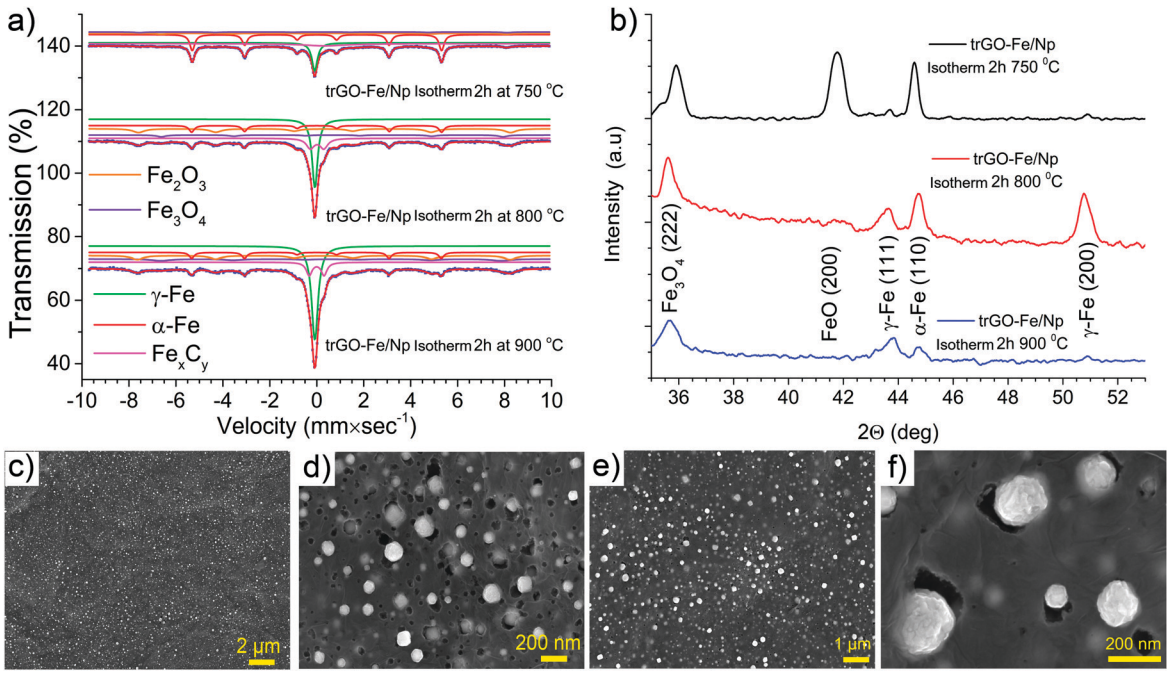

Fig. 4 Characteristics of the tpGO–Fe composites obtained by annealing at varying temperatures. (a) Mössbauer spectra of tpGO–Fe/NP obtained by annealing at 750, 800 and 900 °C for 2 hours, (b) XRD spectra of tpGO–Fe/NP obtained by annealing at 750, 800 and 900 °C for 2 hours, (c and d) SEM images of tpGO–Fe/NP obtained by annealing at 800 °C for 2 hours at different magnification, and (e and f) SEM images of tpGO–Fe/NP obtained by annealing at 900 °C for 2 hours at different magnification.

In tpGO–Fe/NP-750, the content of γ-Fe is significantly lower than α-Fe. Apparently, this temperature is not sufficient to dissolve the needed amount of carbon in α-Fe to form the Fe_xC_y solid solution according to eqn (2).

At temperatures <250 °C, carbon monoxide, a co-product of GO decomposition, can serve as a reducing agent. However, at >700 °C, only the solid tpGO framework can serve as the carbon source. Areas of consumed tpGO are clearly visible around the Fe-NPs in the SEM images (Fig. 4d and f). With increasing the temperature, the solubility of carbon in iron increases significantly. The Fe_xC_y solid solution is formed much more easily, and most of the α-Fe phase is converted to Fe_xC_y. During the cooling process, Fe_xC_y is converted to γ-Fe. Our data confirms that at 800 °C the γ-Fe phase is formed predominantly by eqn (2). A further increase in temperature leads to the acceleration of all processes, and in tpGO–Fe-NP-900 the formation of γ-Fe occurs simultaneously according to eqn (2) and (3).

The role of the time of annealing

The formation of the γ-Fe phase is primarily due to the diffusion of carbon in and out of the transforming nanoparticle. This process is rather slow. That is why the next part of the work was devoted to investigating the role of the time of annealing. The annealing temperature was fixed at 800 °C. This temperature is selected due to three key factors. First is that the natural α-Fe to γ-Fe transition occurs at 917 °C. By subjecting the material to thermal treatment at 800 °C, we exclude completely the natural α-Fe to γ-Fe transition. Thus, all the γ-Fe registered in the sample will be formed by alternative mechanisms. Secondly, the previous experiment (Fig. 4 and Table 2) demonstrated that γ-Fe is formed with comparable yields at temperatures 800 and 900 °C. Finally, the third factor is the possibility of growing substrate-oriented NPs, registered only at 800 °C.

In the new experiment, four different samples were prepared from the same precursor by annealing for 2, 4, 8, and 10 hours. Increasing the time of annealing results in the increase of the yield of the target product. The Mössbauer spectra (Fig. 5a–d and Table 3) clearly show a decrease in the content of both oxides and α-Fe with the time of annealing. In general, an increase in the time of annealing from 2 to 10 hours increases the content of γ-Fe from 40% to 65% (Table 3). In the 10 h annealed sample, the content of α-Fe is only 16%, and no oxides are registered.

Unlike our previous work,[12] in which a high γ-Fe content was attained by heating above the 917 °C transition threshold,

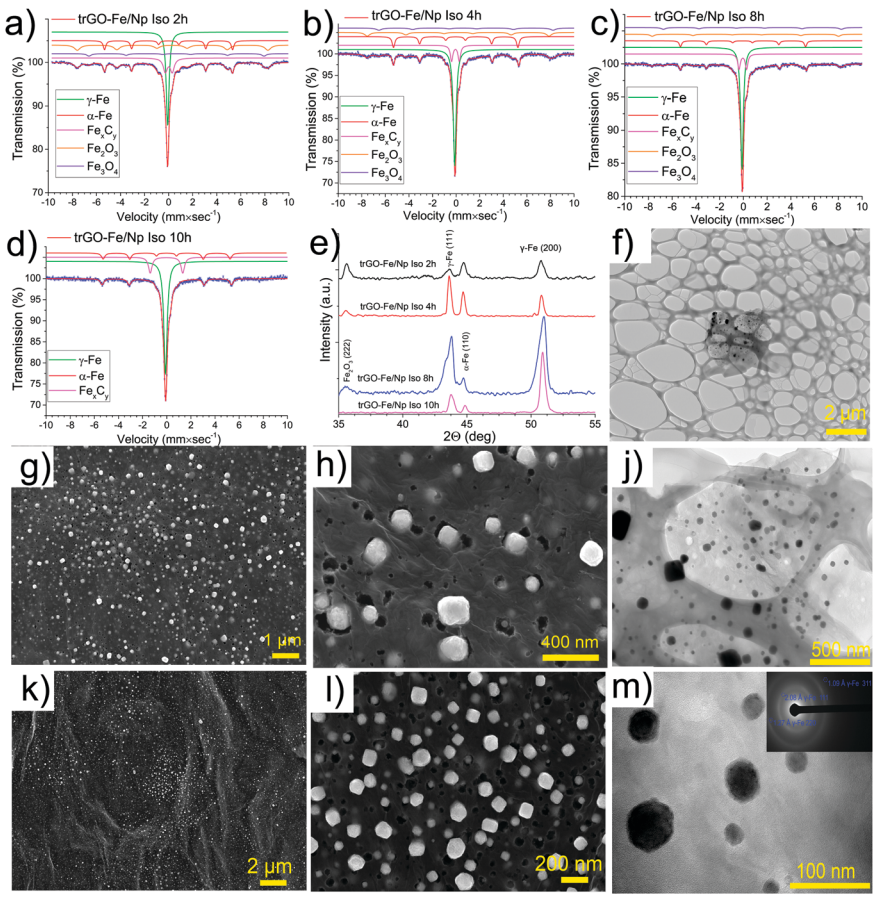

Fig. 5 Characteristics of the tpGO–Fe composites obtained by annealing for varying time. (a–d) Mössbauer spectra of tpGO–Fe/NP after annealing at 800 °C for 2, 4, 8 and 10 hours respectively; (e) XRD patterns of tpGO–Fe/NP after annealing at 800 °C for 2, 4, 8 and 10 hours; (g and h) SEM image of tpGO–Fe/NP after annealing at 800 °C for 8 hours; (k and l) SEM image of tpGO–Fe/NP after annealing at 800 °C for 10 hours; and (f, j and m) TEM images with electron diffraction of tpGO–Fe/NP obtained by annealing at 800 °C for 10 hours.

Table 3 The content of different types of iron in GO/Fe^{3+} samples annealed for different times according to the Mössbauer spectroscopy data (%)

	γ-Fe	α-Fe	Fe_xC_y	Fe_3O_4	Fe_2O_3
2 hour isotherm	40	16	15	6	23
4 hour isotherm	48	12	12	10	18
8 hour isotherm	57	16	13	5	9
10 hour isotherm	65	16	19	—	—

in this study γ-Fe is formed directly from the oxides. In addition, for the samples obtained with 2 h, 8 h and 10 h annealing, formation of the specifically oriented face-centered iron nanoparticles was observed (Fig. 5e): with increasing the annealing time, the intensity of the (200) signal at 50.8 2Θ steadily increases (Fig. 5e). In the case of the stabilization of γ-Fe-NPs formed by the natural alpha-to-gamma transition above the 917 °C temperature threshold, the standard distribution of the (111) and (200) signal intensities was observed.[12] The unusually high (200) signal intensity as compared to the (111) signal suggests the specific orientation of the as-grown nanocrystals, which is induced by the substrate.

The specific orientation is also confirmed by the SEM images (Fig. 5g, h and k, l). After 10 hour annealing, the main part of the products is in the form of cubic nanocrystals. Note that cubic-shaped crystals are most often Miller-index (100), and it is extremely difficult to obtain cubic-shaped crystals exhibiting the second-order diffraction reflex (Fig. 5e).[34]

Based on the TEM images (Fig. 5f, j and m), only core–shell type structures are observed in the sample obtained after 10 hour annealing. At the same time, in the electron diffraction patterns, taken simultaneously from 5 particles, there are only reflexes of γ-Fe, suggesting that the shell of these particles is amorphous. The Mössbauer spectroscopy data (Fig. 5d) clearly indicate that only the Fe_xC_y phase is present in the sample beside γ-Fe. Subsequently, it is straightforward to conclude that the amorphous shell is Fe_xC_y. A schematic of the effect of all the studied factors on the formation of the γ-Fe phase is presented in Fig. 6.

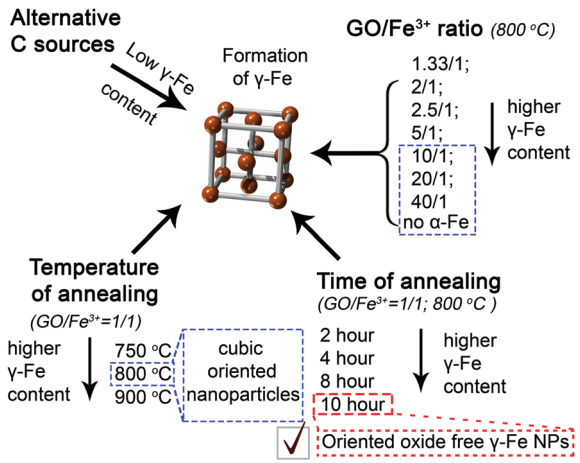

Fig. 6 Schematic description of the main factors leading to the formation of the γ-Fe phase.

Conclusions

The three-dimensional forms of carbon, in both original and oxidized forms, as a structural support do not afford formation of the γ-Fe phase. This observation demonstrates the unique role of GO in the formation of γ-Fe. The oxygen functional groups of GO afford uniform placement of iron ions and nucleation centers on the GO surface. The shift of the GO/Fe^{3+} ratio towards GO increases the yield of γ-Fe. At high GO/Fe^{3+} ratios, γ-Fe is formed without the α-Fe byproduct. However, the product contains significant amount of oxides, formed presumably by oxidation of small-size γ-Fe-NPs when the sample is exposed to air. The yield of γ-Fe increases with both annealing temperature and time. The most efficient growth of the γ-Fe nanoparticles occurs at 800 °C. The increase in the time of annealing up to 10 hours allows one to obtain the most pure γ-Fe product, which does not contain α-Fe and oxides. The unique role of GO as an orienting template for the growth of particles was found. Cube-shaped γ-Fe-NPs lying flat on a tpGO substrate are registered. According to the XRD data, the particles are oriented in the (200) plane. The mechanism of the γ-Fe formation studied in this work is different from the natural α-Fe to γ-Fe transition at 917 °C and subsequent stabilization of as-formed γ-Fe that was reported earlier.

Conflicts of interest

There are no conflicts to declare.

Acknowledgements

This work is supported by the Russian Science Foundation, grant # 16-13-10291.

Notes and references

1 Y. Wang, Z. Yue, Y. Wang, J. Zhang and K. Gao, *Mater. Lett.*, 2018, **219**, 51–54.
2 I. S. Lityaeva, N. V. Bulina, E. A. Petrakovskaya, A. V. Marachevsky, S. M. Zharkov, A. Gedanken and G. N. Churilov, *Fullerenes, Nanotubes, Carbon Nanostruct.*, 2006, **14**, 499–502.
3 N. Yan, X. Zhou, Y. Li, F. Wang, H. Zhong, H. Wang and Q. Chen, *Sci. Rep.*, 2013, **3**, 3392.
4 H. Sadegh, R. Shahryari-ghoshekandi and M. Kazemi, *Int. Nano Lett.*, 2014, **4**, 129–135.
5 L. McCafferty, V. Stolojan, S. G. King, W. Zhang, S. Haq and S. R. P. Silva, *Carbon*, 2015, **84**, 47–55.
6 Y. Cao, *Fullerenes, Nanotubes, Carbon Nanostruct.*, 2015, **23**, 623–626.
7 M. Moazzen, A. Mousavi Khaneghah, N. Shariatifar, M. Ahmadloo, I. Eş, A. N. Baghani, S. Yousefinejad, M. Alimohammadi, A. Azari, S. Dobaradaran, N. Rastkari, S. Nazmara, M. Delikhoon and G. Jahed Khaniki, *Arabian J. Chem.*, 2019, **12**, 476–488.
8 J. Lin, A.-R. O. Raji, K. Nan, Z. Peng, Z. Yan, E. L. G. Samuel, D. Natelson and J. M. Tour, *Adv. Funct. Mater.*, 2013, **24**, 2044–2048.

9 K. Takahashi, Y. Wang, S. Chiba, Y. Nakagawa, S. Isobe and S. Ohnuki, *Sci. Rep.*, 2014, **4**, 4598.
10 J. Guo, R. Wang, W. W. Tjiu, J. Pan and T. Liu, *J. Hazard. Mater.*, 2012, **225–226**, 63–73.
11 A. A. Khannanov, A. R. Valimukhametova, A. G. Kiiamov, I. R. Vakhitov and A. M. Dimiev, *ChemistrySelect*, 2017, **2**, 10546–10554.
12 A. Khannanov, A. Kiiamov, A. Valimukhametova, D. A. Tayurskii, F. Börrnert, U. Kaiser, S. Eigler, F. G. Vagizov and A. M. Dimiev, *J. Am. Chem. Soc.*, 2018, **140**, 9051–9055.
13 P. Tancredi, O. Moscoso Londoño, P. C. Rivas Rojas, M. Knobel and L. M. Socolovsky, *Mater. Res. Bull.*, 2018, **107**, 255–263.
14 R. R. Amirov, J. Shayimova, Z. Nasirova and A. M. Dimiev, *Carbon*, 2017, **116**, 356–365.
15 A. M. Dimiev and J. M. Tour, *ACS Nano*, 2014, **8**, 3060–3068.
16 S. M. Alatalo, E. Daneshvar, N. Kinnunen, A. Meščeriakovas, S. K. Thangaraj, J. Jänis, D. C. W. Tsang, A. Bhatnagar and A. Lähde, *Chem. Eng. J.*, 2019, 821–830, DOI: 10.1016/j.cej.2019.05.118.
17 A. Valimukhametova, A. Khannanov, A. Kiiamov, I. Vakhitov, I. Gilmutdinov, F. G. Vagizov and A. M. Dimiev, *CrystEngComm*, 2019, **21**, 4092–4097.
18 V. Harnchana, S. Chaiyachad, S. Pimanpang, C. Saiyasombat, P. Srepusharawoot and V. Amornkitbamrung, *Sci. Rep.*, 2019, **9**, 1494.
19 R. A. McCurrie, *Ferromagnetic Materials: Structure and Properties*, Academic, 1994.
20 N. G. Gallegos, M. V. Cagnoli, J. F. Bengoa, A. M. Alvarez, A. A. Yeramián and S. G. Marchetti, in *Studies in Surface Science and Catalysis*, ed. R. Aiello, G. Giordano and F. Testa, Elsevier, 2002, vol. 142, pp. 525–532.
21 S. G. Marchetti, M. V. Cagnoli, A. M. Alvarez, J. F. Bengoa, N. G. Gallegos, A. A. Yeramián and R. C. Mercader, *Hyperfine Interact.*, 2002, **139**, 33–40.
22 L. Zhang, X. Yu, H. Hu, Y. Li, M. Wu, Z. Wang, G. Li, Z. Sun and C. Chen, *Sci. Rep.*, 2015, **5**, 90.
23 Y. Wang, Q. He, H. Qu, X. Zhang, J. Guo, J. Zhu, G. Zhao, H. A. Colorado, J. Yu, L. Sun, S. Bhana, M. A. Khan, X. Huang, D. P. Young, H. Wang, X. Wang, S. Wei and Z. Guo, *J. Mater. Chem. C*, 2014, **2**, 9478–9488.
24 X. Huang, Y. Niu and W. Hu, *Colloids Surf., A*, 2017, **518**, 145–150.
25 Y. Niu, X. Huang and W. Hu, *J. Power Sources*, 2016, **332**, 305–311.
26 L. Zhang, X. Yu, H. Hu, Y. Li, M. Wu, Z. Wang, G. Li, Z. Sun and C. Chen, *Sci. Rep.*, 2015, **5**, 9298.
27 X. S. Lv, Y. Qiu, Z. Y. Wang, G. M. Jiang, Y. T. Chen, X. H. Xu and R. H. Hurt, *Environ. Sci.: Nano*, 2016, **3**, 1215–1221.
28 X. Zhang, Q. Yan, J. Li, I. W. Chu, H. Toghiani, Z. Cai and J. Zhang, *Polymers*, 2018, **10**, 183.
29 A. Khasanov, J. He, J. Gaillard, K. Yang, A. M. Rao, C. M. Cameron, J. M. Schmeltzer, J. G. Stevens and A. Nath, *Appl. Phys. Lett.*, 2008, **93**, 1086–1090.
30 A. Khannanov, V. V. Nekljudov, B. Gareev, A. Kiiamov, J. M. Tour and A. M. Dimiev, *Carbon*, 2017, **115**, 394–401.
31 S. E. Habas, H. Lee, V. Radmilovic, G. A. Somorjai and P. Yang, *Nat. Mater.*, 2007, **6**, 692.
32 X. Huang, Z. Zeng, S. Bao, M. Wang, X. Qi, Z. Fan and H. Zhang, *Nat. Commun.*, 2013, **4**, 1444.
33 F.-R. Fan, D.-Y. Liu, Y.-F. Wu, S. Duan, Z.-X. Xie, Z.-Y. Jiang and Z.-Q. Tian, *J. Am. Chem. Soc.*, 2008, **130**, 6949–6951.
34 A. G. Jackson, *Handbook of Crystallography: For Electron Microscopists and Others*, Springer, New York, 2012.